Advanced Functional Materials

ADVANCED FUNCTIONAL MATERIALS
www.afm-journal.de

RESEARCH ARTICLE OPEN ACCESS

How the Carrier Mobility and Seebeck Coefficient of Doped Semiconducting Polymers Are Controlled by Counterion Interactions and Mesoscale Order

Quynh M. Duong[1] | Diego Garcia Vidales[1] | Xinyu Liu[1] | Charlene Z. Salamat[1] | Austin Ready[1] | Hashim Al Khunaizi[1] | Mei Matsumoto[1] | Alexander M. Spokoyny[1] | Sarah H. Tolbert[1,2] | Benjamin J. Schwartz[1]

[1]Department of Chemistry and Biochemistry, University of California, Los Angeles, Los Angeles, California, USA | [2]Department of Materials Science and Engineering, University of California, Los Angeles, Los Angeles, California, USA

Correspondence: Sarah H. Tolbert (tolbert@chem.ucla.edu) | Benjamin J. Schwartz (schwartz@chem.ucla.edu)

Received: 15 January 2026 | **Revised:** 9 April 2026 | **Accepted:** 13 April 2026

ABSTRACT

Charge transport/structure relationships in chemically-doped poly(3-hexylthiophene-2,5-diyl) (P3HT) films are explored using four different dopants: the classic 2,3,5,6-tetrafluoro-7,7,8,8-tetracyanoquinodimethane (F_4TCNQ) as well as two large dodecaborane (DDB) cluster-based dopants that minimize counterion Coulomb interactions with carriers on the polymer backbone. Anion-exchange doping with F_4TCNQ and lithium bis(trifluoromethane)sulfonimide (LiTFSI) was also used to put $TFSI^-$ counterions into the doped polymer. The Seebeck coefficient (S) and conductivity (σ) were measured as a function of doping level, along with temperature-dependent conductivity, wide- and small-angle x-ray scattering, optical spectroscopy, and Hall effect mobility. The results indicate that large DDB-based counterions produce lower carrier transport activation energies and thus more favorable S-σ relationships than F_4TCNQ. Anion-exchange doping leads to higher activation energies but still produces a favorable S-σ relationship. Analysis using the semi-localized transport (SLoT) model indicates that anion-exchange doping produces films with the highest intrinsic conductivities, which results from doping-induced crystallization of originally amorphous regions of the film. Such crystallization leads to increased mesoscale domain sizes, as observed by small-angle X-ray scattering. Together, the results indicate that transport in doped conjugated polymers can be equivalently improved either by reducing the Coulomb interaction of carriers with counterions or by structurally improving mesoscale conductivity pathways.

1 | Introduction

Doped semiconducting polymers have great potential promise for thermoelectric applications due to their ease of processing, chemical tunability, and inherently low thermal conductivity [1–4]. Interest in these materials has increased in recent years with the development of new polymers, dopants, and doping methods [5–10]. Most of the work in this field focuses on improving the electrical conductivity of semiconducting polymers by overcoming their intrinsically low carrier mobility and density via doping, which creates mobile carriers on the polymer backbone. For thermoelectric devices, it is also crucial to consider the Seebeck coefficient, which is the voltage difference generated in response to a temperature gradient across a material. This voltage facilitates the flow of charge carriers, enabling the direct conversion of waste heat into electrical energy.

Quynh M. Duong and Diego Garcia Vidales contributed equally to this work.

The efficiency of the thermoelectric conversion process is described by the figure of merit, ZT:

$$ZT = \frac{\sigma S^2}{\kappa} T \tag{1}$$

which depends on the electrical conductivity (σ), Seebeck coefficient (S), and thermal conductivity (κ). The temperature (T) is included to make the quantity dimensionless. Although it is desirable to maximize both the electrical conductivity and the Seebeck coefficient to achieve higher ZT, increasing the electrical conductivity through doping generally results in a decrease in the Seebeck coefficient. This inverse relation leads to a sweet spot in choosing the doping level to maximize the numerator of Equation (1), which is also referred to as the power factor.

The inverse relationship between σ and S can be understood using the Boltzmann transport formalism. In the version developed by Kang and coworkers, these factors are described in terms of a transport function, σ_E, which is related to the carrier mobility [11]:

$$\sigma = \int \sigma_E \left(-\frac{\partial f}{\partial E}\right) dE \tag{2}$$

$$S = -\frac{k_B}{q} \int \left(\frac{E - E_F}{k_B T}\right) \left(\frac{\sigma_E}{\sigma}\right) \left(-\frac{\partial f}{\partial E}\right) dE \tag{3}$$

where k_B is the Boltzmann constant, E is the energy of the charge carrier, q is the fundamental charge, E_F is the Fermi level, and $f(E)$ is the Fermi-Dirac distribution. Although not explicit in these equations, increasing the conductivity by increasing the carrier density shifts the Fermi level into the band, thereby reducing the asymmetry in σ_E about E_F and lowering the average value of $(E - E_F)$ for the carriers that contribute to the Seebeck coefficient [11]. This explains why the Seebeck coefficient decreases when the electrical conductivity increases at higher doping levels [12–16].

The electrical conductivity of a doped conjugated polymer depends not only on the number density of carriers but also on the carrier mobility: higher carrier mobility results in higher conductivity at the same carrier density. Equations (2 and 3) indicate that doped semiconducting polymers that have higher carrier mobilities also will have higher Seebeck coefficients relative to their electrical conductivity [17, 18], thus leading to an improved power factor and ZT.

Charge transport in doped semiconducting polymer films is typically understood as a hopping process, where carriers must thermally surmount a barrier in order to move. This process is influenced by several factors, including structural disorder and the Coulomb interactions between polarons and their counterions, both of which create barriers that trap charge carriers at specific locations. Temperature also plays a key role in this transport: at higher temperatures, polarons gain enough thermal energy to surmount these energy barriers. In order to improve the carrier mobility in doped semiconducting polymers, it is necessary to understand how the interplay of all of these factors contributes to charge transport [8, 9, 12, 16, 19–22].

Recently, Gregory and coworkers [17, 18] expanded on the transport model developed by Kang and coworkers [11] by proposing that the charge transport function takes the following form:

$$\sigma_E\ (E, T, c) = \sigma_0 \exp\left(-\frac{W_H(c)}{k_B T}\right) \times \left(\frac{E - E_t}{k_B T}\right) \tag{4}$$

This expression for the transport function is termed the semi-localized transport (SLoT) model, which introduces three components: σ_0, the pre-factor or intrinsic conductivity in the absence of localization effects; $W_H(c)$, a localization energy that depends on the carrier density (c), which represents the energy that carriers must overcome to hop between sites; and an energy-dependent term, $(\frac{E-E_t}{k_B T})$. By assuming that the material is homogeneous throughout its volume, $W_H(c)$ can further be broken down into a maximum localization energy ($W_{H,max}$) and the (presumed linear) rate at which the localization energy decreases with increasing carrier density ($W_{H,slope}$). Thus, by using temperature-dependent conductivity measurements to extract the activation energy, in combination with Equation 4, one can determine whether charge transport is primarily influenced by σ_0 or by $W_H(c)$ upon doping. Our goal in this work is to determine how these factors depend on both the microscopic and mesoscopic morphology of the doped polymer films.

Different dopants and doping methods are well known to significantly influence the morphology of doped polymer films [8, 9, 12, 16, 19–30]. These morphological changes can occur on microscopic length scales, such as changes in crystallite structure, as well as on mesoscopic scales, leading to variations in domain length [8, 9, 12, 16, 19–25, 27, 30]. Such structural variations can lead to significant differences in the charge transport properties of doped semiconducting polymer films. In this study, we explore how different dopants and doping methods affect morphology and thus charge transport in doped semiconducting polymers. Specifically, we measure the electrical conductivity, Seebeck coefficient, and activation energy (W_H), and then use the SLoT model to analyze charge transport in terms of parameters such as σ_0 and $W_H(c)$. We then interpret the results using both small- and wide-angle X-ray scattering experiments to reveal how the morphology induced by different doping methods affects the S-σ relationship.

To investigate how different dopants and doping methods influence charge transport and the S-σ relationship, we focus on the workhorse semiconducting polymer poly(3-hexylthiophene-2,5-diyl) (P3HT) [20, 31–39]. P3HT is a semicrystalline polymer containing both crystalline and amorphous regions. The lack of order in the amorphous regions leads to shorter average conjugation lengths and thus higher oxidation potentials; in other words, amorphous regions can be up to a few hundred meV harder to dope than crystalline regions [40]. We then choose dopants and doping methods that have different effects on film morphology, including: where the counterion sits in the polymer crystal structure, whether or not the method enhances or destroys overall crystallinity, and whether or not the dopant can create carriers only in the crystalline regions or in both the crystalline and amorphous regions. Figure 1 shows the chemical structures of the semiconducting polymer and dopants used in this study.

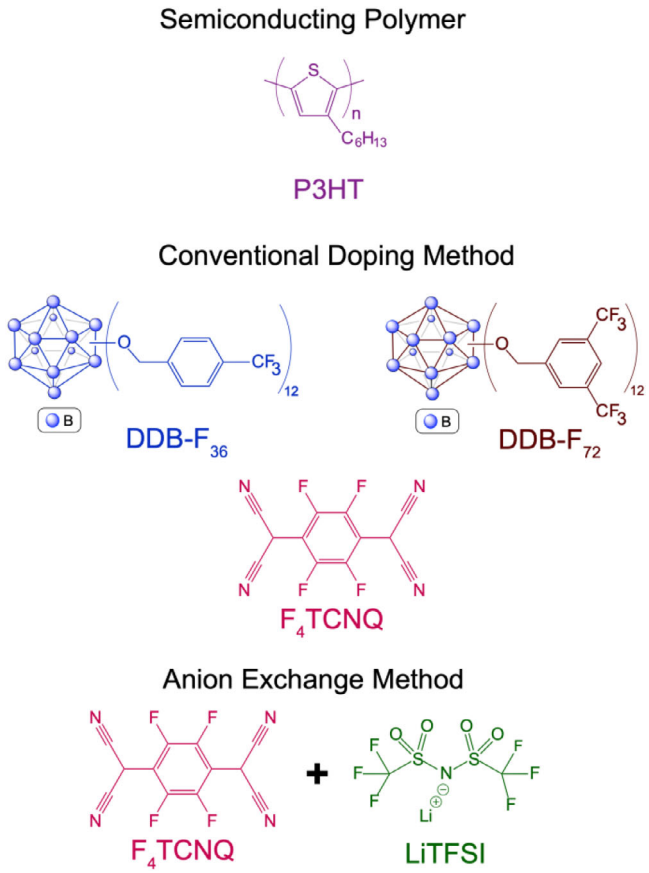

FIGURE 1 | Chemical structures of P3HT and the various dopants used in this study. Two doping methods are used in this study: conventional and anion-exchange. For the conventional doping method, we utilize three dopants: F_4TCNQ, DDB-F_{36}, and DDB-F_{72}, which vary in oxidizing power from weakest to strongest, respectively. The weakest dopant, F_4TCNQ, is primarily able to dope only crystalline regions of P3HT. The two boron cluster dopants are stronger oxidants, and although the oxidation power difference between the DDB-F_{36} and DDB-F_{72} dopants is ~200 mV, their equally large counterions reside in the lamellae in the polymer lattice upon doping. For the anion-exchange method, the dopant is F_4TCNQ and the electrolyte is LiTFSI. The anion-exchange doping method allows for control over the nature of the dopant's counterion, and the presence of the electrolyte provides an extra oxidative boost, allowing doping of both amorphous and crystalline regions in the polymer matrix.

For our initial dopant, we chose 2,3,5,6-tetrafluoro-7,7,8,8-tetracyanoquinodimethane (F_4TCNQ) because it is widely used in studies of doped semiconducting polymers [9, 16, 41–45]. The doping efficiency of F_4TCNQ and the regions of P3HT it can dope depend strongly on the doping procedure, the choice of solvent used for doping, and the dopant concentration [8, 21, 22, 43, 46–48]. Under sequential doping conditions at high-doping concentrations in relatively high-swelling solvents like dichloromethane (DCM), which is what we will use in this work, F_4TCNQ has sufficient oxidizing power to dope the crystalline regions of P3HT without significantly doping the amorphous regions [8, 21, 22, 43, 48].

When doping P3HT with F_4TCNQ, which occurs via integer charge transfer (ICT), the F_4TCNQ^- counterions typically reside in the lamellar regions of the P3HT crystallites, nestled among the hexyl side chains. With some processing conditions, the addition of F_4TCNQ to P3HT can produce charge-transfer complexes (CTCs), where the F_4TCNQ^- anion π-stacks with the P3HT backbone; CTCs have only partial charge transfer and thus are not associated with mobile carrier formation [48, 49]. Even when creating carriers via ICT, however, the relatively strong Coulomb interactions between polarons and the F_4TCNQ^- counterions in the crystalline lamellae promote carrier localization [20], resulting in a substantial population of trapped charge carriers [9, 20, 50].

In addition to F_4TCNQ, we also explore using dodecaborane (DDB) cluster-based dopants, whose large ~2-nm-diameter size leads to reduced Coulomb interactions, resulting in more mobile charge carriers [8, 9, 51]. DDBs can be modified with different substituents to change their oxidation power [8, 9, 51]. The two dopants we use in this work, DDB-F_{72} and DDB-F_{36}, are named based on the total number of fluorine atoms on each cluster. Although both DDB-based dopants help minimize Coulomb trapping, DDB-F_{72} can dope amorphous regions of P3HT films more effectively than DDB-F_{36} due to its ~200 mV stronger oxidization power. The large size and strong oxidizing power of DDB-F_{72}, however, play a direct role in the P3HT film's morphology: our previous work has shown that the intercalation of DDB-F_{72} dopant in the P3HT film disrupts the film's crystallinity at high doping concentrations. This is not the case when DDB-F_{36} is used to dope P3HT, where we have shown that doped films retain their degree of crystallinity but with a crystal structure that has a significantly expanded lamellar distance [9, 51]. By employing both dopants, we are thus able to keep local counterion-polaron Coulomb interactions constant, giving us a direct handle for understanding the trade-off between doping-induced structural disorder and dopant accessibility to different regions of the film, and how these factors influence charge transport characteristics.

Recently, Yamashita and colleagues developed a new technique called anion-exchange (AE) doping, which offers several benefits over traditional chemical doping methods [6]. The AE approach involves immersing a conjugated polymer film into a solution containing both a chemical dopant and a high concentration of an electrolyte in a semi-orthogonal solvent, which swells the polymer film without dissolving it, thereby facilitating intercalation of the dopant and electrolyte ions into the polymer. Anion-exchange doping proceeds through a two-step process: first, the dopant oxidizes the polymer, and second, the dopant counterion is replaced by the electrolyte anion through mass action. This method not only allows for control over the choice of counterion in doped polymer films, but it also boosts the doping power by ~200 mV, thereby enabling higher doping levels than conventional methods [6]. In this study, we take advantage of this oxidative boost by using F_4TCNQ, which predominantly dopes crystalline regions, together with lithium bis(trifluoromethanesulfonyl)imide (LiTFSI) as the electrolyte salt, to dope both the crystalline and amorphous regions in P3HT films. Since doping the amorphous regions can lead to significant structural changes, we can then investigate how these structural changes relate to charge transport and the *S*-σ relationship.

Thus, in this study, we examine how different dopants – F_4TCNQ, DDB-F_{72}, and DDB-F_{36} – and different doping methods

– conventional and anion exchange – affect the morphology, charge transport, Seebeck coefficient, and electrical conductivity of doped P3HT. Our findings show that charge transport, and thus the Seebeck coefficient-electrical conductivity (S-σ) relationship, can be improved either by reducing Coulomb trapping or by increasing mesoscale ordering through the crystallization of formerly amorphous regions. Using a combination of temperature-dependent conductivity and Hall effect measurements, along with UV–vis–NIR spectroscopy, we demonstrate that P3HT films doped with DDB-based dopants exhibit much less carrier localization compared to those doped with F_4TCNQ or via the anion-exchange method due to the reduced counterion-polaron interaction. Additionally, using the SLoT model, we find that doping by anion exchange produces a significantly higher σ_0 than conventional doping, allowing charge carriers to overcome their increased localization and achieve charge transport and Seebeck coefficient-electrical conductivity relationships that are similar to those of DDB-doped films, where the carriers have much lower activation energy. Furthermore, Grazing-Incidence Wide- and Small-Angle X-ray Scattering (GIWAXS and GISAXS) analyses reveal that the high σ_0 observed in anion-exchange doped films is due to an increase in mesoscale domain length that results from doping and ordering of the amorphous regions. Overall, our work emphasizes the key role that dopants and doping methods play in the thermoelectric efficiency of doped conjugated polymers: by controlling key factors such as dopant size and oxidizing power, we can deconvolute the different doping-induced structural and energetic disorder governing the charge transport characteristics of doped conjugated polymers.

2 | Results and Discussion

As mentioned above, the goal of this study is to examine dopant-induced structural changes in P3HT to better understand the relationship between morphology and charge transport characteristics in doped semiconducting polymer systems. To deconvolute the role of morphology in the charge transport characteristics of doped P3HT, we control not only the dopant size and shape, but also the oxidizing power that determines which regions of the polymer film can be doped. To fabricate the doped semiconducting polymer P3HT films for this study, we used the sequential processing (SqP) method [52–55]. First, P3HT films were spin-coated onto glass substrates. After the films dried, this was followed by a second spin-coating step with solutions of different dopants, including F_4TCNQ, DDB-F_{72}, and DDB-F_{36}. For anion-exchange doping, we used a dopant solution containing F_4TCNQ as well as 104.5 mM of LiTFSI. Additional details on the materials used, film fabrication techniques, and doping processes can be found in the Experimental section.

2.1 | UV–Vis–NIR Spectroscopy

We start our investigation by performing UV–vis–NIR spectroscopy on P3HT films doped using DDB-F_{72}, DDB-F_{36}, F_4TCNQ, and via anion exchange (AE) at various doping concentrations (Figure 2). For all of the doped samples, we observe an absorption increase at ∼1.5 eV and ∼0.5 eV, the so-called P2 and P1 peaks, respectively, which are associated with the presence of polaronic charge carriers. All of the doped films also show a depletion of the bandgap transition of the neutral polymer near ∼2.3 eV. Both the DDB-F_{72}- and DDB-F_{36}-doped films exhibit a third polaron transition (P3) at ∼1.6 eV that disappears at higher doping levels [8, 9]. The P2 region in F_4TCNQ-doped samples and the bandgap region in the DDB-doped samples also have overlapping absorptions from the dopant anions [8, 45, 51, 55–57]. Despite the peak overlaps, we see that with increasing dopant concentration, both the P1 and P2 intensities rise, indicating the creation of more polarons. In the case of the anion exchange doping method, we also see no absorption signatures of F_4TCNQ^- in the P2 region, indicating that anion exchange occurred.

Based on their similar P1 absorption intensities, which are in a region free of spectral overlap, the F_4TCNQ, DDB-F_{72}, and anion-exchange (F_4TCNQ with LiTFSI) doped P3HT films have similar doping levels at dopant concentrations of 3.62 mM, 0.5 mM, and 3.62 mM with 104 mM LiTFSI, respectively. DDB-F_{72} is clearly more efficient at doping, as it reaches the same level of doping at a solution concentration ∼7 times lower than that of the other dopants. In contrast, DDB-F_{36} is less effective at doping P3HT than DDB-F_{72}, showing a much lower P1 intensity even at twice the doping concentration; it also appears slightly less effective at doping P3HT than F_4TCNQ.

Based on cyclic voltammetry, DDB-F_{36} is slightly more oxidizing than F_4TCNQ [8], which would typically suggest a higher doping efficiency. However, solution-phase redox potentials may not necessarily translate directly to doping efficiency, where ion pairing effects, the local dielectric environment of the solvent-swollen film, and dopant intercalation can strongly influence charge transfer and stabilization of the resulting ionized species and thus the doping levels achieved. In the case of DDB-F_{36}, its large size likely makes it more difficult to intercalate into the polymer lattice during SqP, even in high-swelling solvents like DCM, leading to a lower doping level.

In addition to providing qualitative insights into doping level, the spectral position of the P1 absorption also reveals important details about charge carrier delocalization. Although a detailed assignment of the P1 transition is still the subject of discussion in the literature, recent experimental and theoretical work from our group and others supports a description in which the P1 transition corresponds to excitation from the valence band into a partially-filled polaronic intragap state in doped P3HT [19, 58–63]. Theoretical work by Spano and co-workers has argued that a red-shifted P1 transition is associated with greater carrier delocalization, whereas a blue-shifted P1 indicates stronger localization [8, 9, 21, 64]. We have argued previously that there is a correlation between the molecular-level degree of localization and the macroscopic carrier mobility [8, 9], but others have pointed out that this correlation is not perfect [28, 30], and one of the purposes of this paper is to explore carrier transport on length scales between the molecular and macroscopic.

The observation that the position of the P1 absorption band reflects localization of the polaron due to Coulomb interactions with the dopant counterion explains why P3HT films doped with DDB-F_{72} and DDB-F_{36} exhibit a significant P1 redshift compared to those doped with F_4TCNQ or via AE. This is because the larger size of the DDB dopants forces the charge of the counterion to be positioned further from the polymer backbone than is

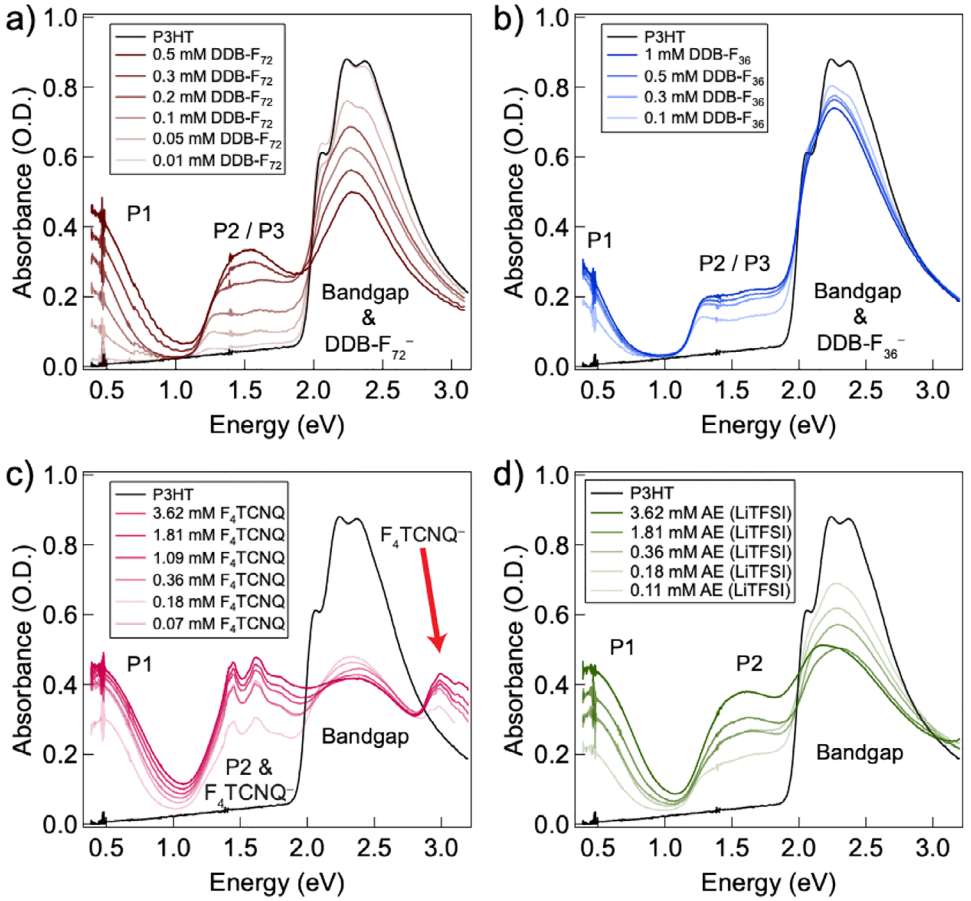

FIGURE 2 | UV–vis–NIR spectra of doped P3HT films using different dopants/methods: (a) DDB-F_{72}, (b) DDB-F_{36}, (c) F_4TCNQ, and (d) anion exchange (AE) at various doping levels. All four doping methods produce the P1 and P2 absorption bands characteristic of polarons, as well as decrease the absorption intensity of the P3HT bandgap. The bandgap bleach is less apparent for the two DDB dopants because the DDB anions absorb near 2.4 eV, overlapping the P3HT bandgap transition. The vibronic structure near 1.5 eV and the peak near 3.0 eV in panel (c) come from the F_4TCNQ anion. The legend in the anion exchange samples shows the final F_4TCNQ concentrations. The LiTFSI concentration was kept constant at 104.5 mM.

the case for smaller counterions, such as $TFSI^-$ or F_4TCNQ^- [8]. This increased distance weakens the Coulomb interaction, leading to more delocalized carriers and thus a red-shifted P1 band [50]. In contrast, the P1 transition for films doped with the anion-exchange method is at a similar position to that of F_4TCNQ-doped films, with both showing a bluer P1 transition. This similarity in P1 peak position suggests that the counterion Coulomb interactions, and thus the degree of carrier localization, in anion-exchange doped P3HT films are comparable to those in F_4TCNQ-doped films.

2.2 | Probing Film Morphology Using Grazing Incidence Wide- and Small-Angle X-ray Scattering Techniques

To investigate the different morphologies that result from the various dopants and doping methods used in this study, we structurally characterized the doped semiconducting P3HT polymer films using grazing-incidence wide- and small-angle X-ray scattering (GIWAXS and GISAXS). All films retain their crystallinity upon doping and show the expected edge-on orientation with respect to the substrate, as seen in the raw 2D scattering data (Figure S1). Figure 3a,b displays integrations of the GIWAXS diffraction patterns for the most highly-doped samples shown in Figure 2, with integrations in the out-of-plane and in-plane directions plotted separately. The one exception is the DDB-F_{72} doped film, which is shown for the second-highest doping level, 0.3 mM, because of increased disorder that occurs at the highest doping level. Out-of-plane and in-plane integrations can be found for P3HT doped with all four dopants at all doping levels in Figures S2 and S3.

For the case of F_4TCNQ (red curve, Figure 3a), the data show a shift of the (100) peak, which corresponds to the lamellar spacing of the P3HT crystallites, from approximately 0.39 $Å^{-1}$ to a lower q-spacing of about 0.35 $Å^{-1}$ upon doping. This shift, which has been noted in several studies, indicates that the lamellar region of P3HT is expanding to accommodate the F_4TCNQ anion within the polymer crystal structure [20, 21, 51]. Figure 3b shows that F_4TCNQ doping also causes a shift of the (020) π-stacking peak: this peak moves from approximately 1.65 $Å^{-1}$ to a higher q around 1.70 $Å^{-1}$, indicating a reduction in the π-stacking distance. This shift has been attributed to a reorientation of the π-stacking direction with respect to the unit cell axis, a change that modifies the tilt-angle of the hexyl side chains to make more room for intercalation of counterions into the lamellar region [20, 21, 51].

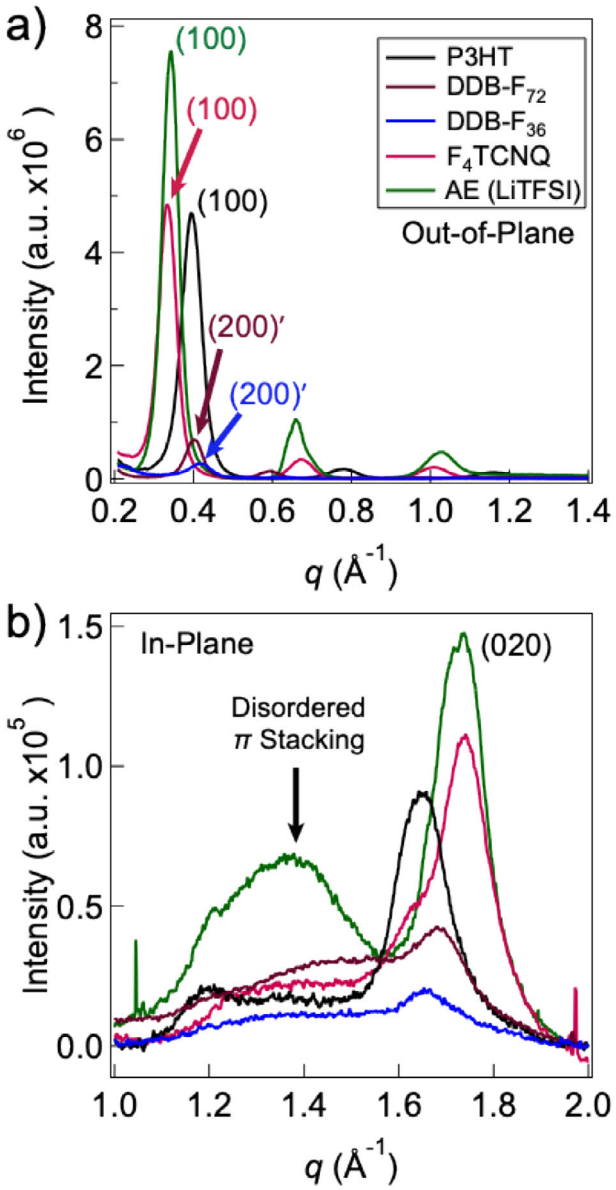

FIGURE 3 | Out-of-plane (panel a) and in-plane (panel b) integrated GIWAXS data for pristine P3HT (black curve) and for the most highly-doped P3HT samples for each dopant shown in Figure 2. Specific dopant concentrations were 1 mM DDB-F_{36}, 3.62 mM F_4TCNQ, and 3.62 mM F_4TCNQ combined with 104.5 mM LiTFSI for the anion exchange sample. For P3HT doped using DDB-F_{72}, the data shown corresponds to the second-highest concentration (0.3 mM), because there is a drop in the electrical conductivity and Hall carrier mobility due to amorphization of the film at the highest doping concentration.

In the out-of-plane GIWAXS integration in Figure 3a, the anion-exchange-doped (green curve) films show a shift in the (100) lamellar peak to approximately 0.35 Å^{-1} [27], resulting in a lamellar spacing similar to that of the F_4TCNQ-doped samples. In the in-plane integration in Figure 3b, the (020) π-stacking peak shifts to a q-spacing of ~1.75 Å^{-1}, a value that is only slightly larger than that observed for the F_4TCNQ-doped materials. The similarity in changes to both the (100) and (020) peaks between anion-exchange doped films and F_4TCNQ doped films suggests that these similarly-sized counterions distort the P3HT crystal lattice in a comparable fashion and that both sit within the lamellar region. Therefore, the hypothesis of roughly similar Coulomb interactions between polarons and each of these anions is consistent with the similar P1 peak positions seen in Figure 2.

Additionally, Figure 3b shows that the anion-exchange-doped P3HT samples have a broad scattering peak centered around ~1.4–1.5 Å^{-1}. Scattering in this region has been previously attributed to partly-ordered π-stacking associated with semi-amorphous regions of doped polymer films [8, 51]. When amorphous polymer regions are doped, they become more ordered, but they are not always able to fully crystallize. Therefore, the presence of this peak suggests that anion-exchange doping is affecting the amorphous regions of the P3HT film and increasing their degree of order to the point where they contribute to the scattering pattern. We note that the AE films were doped using n-butyl acetate (*n*-BA) as the solvent while the other films were doped using dichloromethane (DCM) as the solvent. Thus, to test whether this disordered π-stacking peak was related to the AE doping method or the use of *n*-BA, we performed a series of control experiments where we doped P3HT films with F_4TCNQ from both *n*-BA and DCM. The results are shown in Figure S4, and they make clear that F_4TCNQ-doped P3HT films do not show significant scattering in the disordered π-stacking region upon doping from either solvent (see Supporting Information), indicating that the ~1.4–1.5 Å^{-1} feature observed in the anion-exchange-doped samples is not caused by the solvent alone.

Unlike the F_4TCNQ- and anion-exchange-doped samples, the out-of-plane integrations for the DDB-doped in Figure 3a samples (brown and blue curves) show a significant shift of the (*h*00) peaks to a much lower q-spacing, so low that only the (200) lamellar peak of the doped structure [labeled (200)'] can be observed outside of the beam stop used in the experiment [8]. This expansion is driven by the large size (~2 nm diameter) of the DDB-based counterions, which greatly expand the lattice in the lamellar direction in order to create a larger space into which they can fit. This expansion is what causes the DDB anions to have weaker Coulomb interactions with polarons due to their increased distance from the polymer backbone [9].

In contrast to the significant expansion of the lamellae, the in-plane integration in Figure 3b reveals that the (020) π-stacking peaks for both DDB-F_{72}- and DDB-F_{36}-doped P3HT films show minimal change from the pristine value, suggesting that the original π-stacking morphology is largely preserved; the DDB clusters are so large that they cannot intercalate within the hexyl side chains, as with the F_4TCNQ- and anion-exchange-doped samples, so they instead sit as an independent layer between the hexyl moieties [8]. Although the two DDB-based dopants have largely similar molecular structures, a broad shoulder centered near 1.4–1.5 Å^{-1} appears below the (020) π-stacking peak in DDB-F_{72}-doped films, which is much less pronounced in the DDB-F_{36}-doped films. This broad shoulder could be either a signature of partial doping-induced crystallization of amorphous regions, as mentioned above, or it could correspond to a loss of some of the originally crystalline regions of the film [8, 51]. Since DDB-F_{72} is highly oxidizing, it should dope the amorphous regions, making them more ordered, and heavily dope the crystalline regions to the point where the crystal structure could

TABLE 1 | Radius of gyration (R_g) obtained from GISAXS for P3HT samples doped at similar Hall carrier densities of $\sim 5 \times 10^{20}$ cm^{-3} with different dopants (cf. Figure 5b). The dopant concentrations needed to achieve carrier densities around this level are 0.3 mM DDB-F_{72}, 1 mM DDB-F_{36}, 0.18 mM F_4TCNQ, and 1.81 mM/104.5 mM anion exchange (F_4TCNQ/LiTFSI). The R_g values for all four dopants at all the dopant concentrations studied are presented in Table S1. The R_g values were obtained using the Unified fit model (see Supporting Information for fitting details). Also presented are the σ_0 and $W_{H,slope}$ parameters from the SLoT model fits to the Seebeck coefficient-conductivity data in Figure 4.

	Pristine	F_4TCNQ	AE	DDB-F_{72}	DDB-F_{36}
R_g (Å)	80	57	107/51	39	58
Hall Carrier Density ($\times 10^{20}$ cm^{-3})	—	5.2	4.8	5.1	3.6
σ_0 (S cm^{-1})	—	10	125	25	35
$W_{H,slope}$ (meV)	—	310	350	1000	1550

be partly disrupted due to the large number of DDB clusters that must be inserted into the crystalline lattice. The smaller shoulder at 1.4–1.5 Å^{-1} in the DDB-F_{36}-doped films indicates that this less oxidizing dopant does not dope strongly enough to disrupt the crystallites or significantly re-order amorphous regions.

In addition to changes in the local crystal structure, doping also causes changes on larger length scales, which we probe using GISAXS [65–71]. Table 1 provides the domain size, or radius of gyration (R_g) correlation length, extracted from GISAXS for P3HT thin films doped at a Hall carrier density of $\sim 5 \times 10^{20}$ cm^{-3} for all four dopants (see Figures S6 and S7 for the GISAXS integrations and fits used to obtain R_g for each dopant). A larger R_g is associated with doped domains that persist over a greater distance, likely indicating greater continuity of the conductive pathways within those films [72, 73].

Our GISAXS results reveal that the initial pristine P3HT film has $R_g = 80$ Å, a value that likely corresponds to the crystalline domain sizes within the film. Upon doping with F_4TCNQ, R_g decreases to 57 Å, indicating that the doped domains may be smaller than the original polymer crystallites [12, 29, 74]. Interestingly, both DDB-F_{72}- and DDB-F_{36}-doped films exhibit still lower R_g values, 39 and 58 Å, respectively. The decrease in R_g in the DDB-based P3HT samples can be attributed to the dopant's large size, which should cause significant strain within the polymer network, causing single polymer domains to break up into multiple smaller domains upon doping. Doping-induced crystallization may also result in the formation of new, small, doped polymer domains. The much lower R_g value observed in the DDB-F_{72}-doped P3HT films is likely caused by this latter effect. The less oxidizing DDB-F_{36} dopant has only enough oxidizing power to dope P3HT but not to crystallize the amorphous regions, leading to a smaller change in domain size from the pristine P3HT. In contrast to both the F_4TCNQ- and DDB-doped P3HT films, the GISAXS data show two different correlation lengths for the anion-exchange-doped samples, with R_g values of 51 and 107 Å. The higher R_g value of 107 Å, which exceeds that of the pristine film, likely corresponds to growth of the original domains through the same process of doping-induced crystallization. The smaller R_g signal may arise from new crystalline domains formed through doping-induced crystallization of amorphous regions, where the new domains were not able to grow epitaxially onto existing domains and instead nucleated independently.

Finally, to fully understand the doping-induced structural changes, we also evaluated the paracrystallinity, $g_{(h00)}$, of these samples, shown in Figure S5. We found little overall change in $g_{(h00)}$ upon doping, a result that indicates that $g_{(h00)}$ values do not follow the same trend as R_g. This is because paracrystallinity reflects lattice disorder within the crystallitesP, whereas R_g reflects the larger-scale domain size within the doped films [72, 73]. As domains grow or fracture upon doping, they may do so with retention of crystalline order, or with increased disorder, but grain growth and disorder are not intrinsically coupled.

With this understanding of the P3HT structural changes induced by different dopants, we turn next to address the question: how do these doping-induced morphological changes influence the charge transport characteristics in P3HT doped systems?

2.3 | Seebeck Coefficient-Electrical Conductivity Relationship

Having investigated the local and mesoscopic structure of P3HT doped with DDB-F_{72}, DDB-F_{36}, F_4TCNQ, and via anion exchange, we now turn to investigating how the different doped polymer morphologies affect macroscopic thermoelectric properties such as the Seebeck coefficient and electrical conductivity. To measure the Seebeck coefficient, we deposited two parallel line electrodes onto the film and created a temperature gradient to measure the resulting voltage; the corresponding ΔV versus ΔT data used to extract the Seebeck coefficients are shown in Figure S9. Electrical conductivity was assessed using the Van der Pauw method, with electrodes placed at the four corners of square film samples. More details of how the Seebeck coefficient and electrical conductivity are measured can be found in the Experimental section, and the full conductivity and Seebeck coefficient data as a function of dopant concentration are shown in Figure S8. Figure 4 shows the measured Seebeck coefficient and the electrical conductivity of P3HT doped with all four dopants across various doping levels (the same samples whose absorption spectra are presented in Figure 2). We note that some of the lowest-concentration-doped samples, even though they showed evidence of doping via UV–vis–NIR spectroscopy, had electrical conductivities too low to be accurately measured.

For all of the doped P3HT samples, increased doping improves the conductivity but also shifts the Fermi level deeper into the band, reducing the asymmetry of the transport distribution around E_F

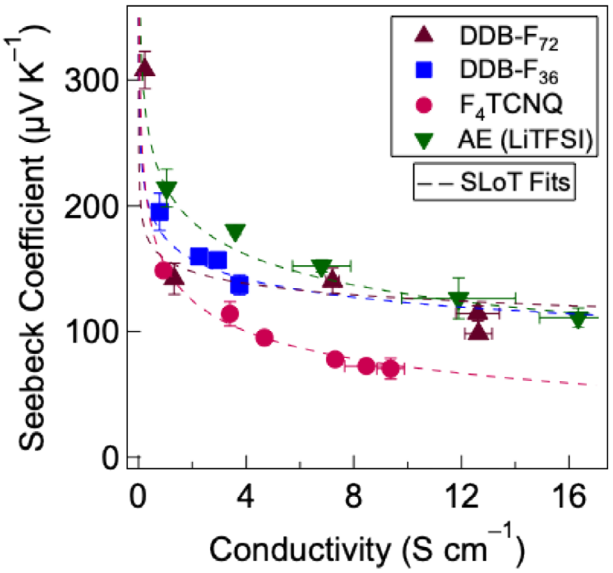

FIGURE 4 | Seebeck coefficient-conductivity (S-σ) relationship for P3HT doped at different levels with various dopants/counterions. The dashed curves are fits to the SLoT model (Equations 2, 3, and 4), with parameters summarized in Table 1 and in the Supporting Information. Both the DDB-based dopants and anion-exchange doping show significantly higher Seebeck coefficients for the same electrical conductivity compared to F_4TCNQ-doped P3HT samples.

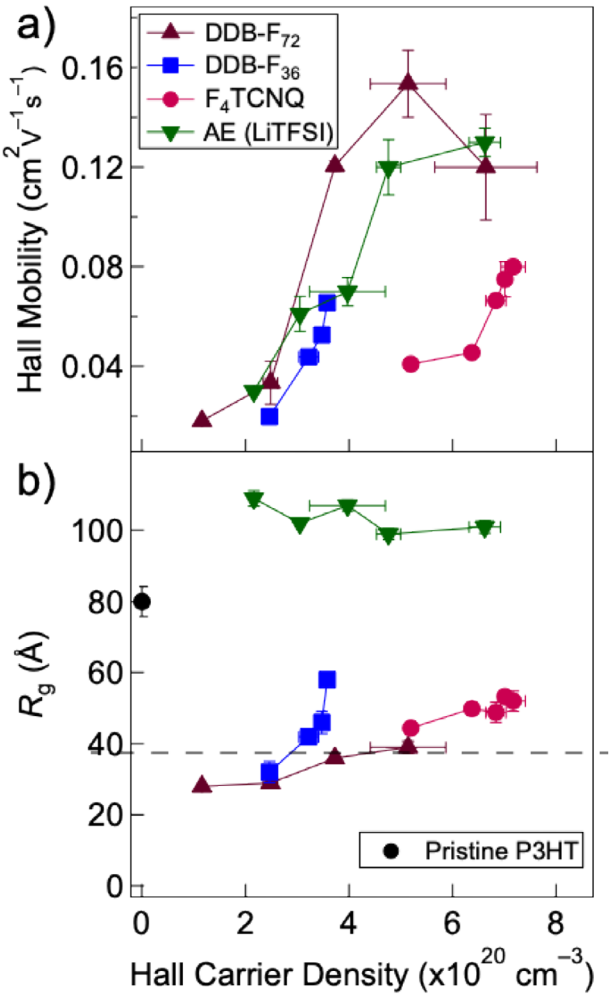

FIGURE 5 | (a) Hall effect measurements for P3HT films doped at different levels with various dopants. The x-axis is the Hall carrier density (rather than dopant concentration) since the different dopants and methods have different doping efficiencies. The DDB-based dopants and anion-exchange method show significantly higher Hall mobility at a given carrier density than the samples doped using F_4TCNQ. Panel (b) shows how the R_g obtained from GISAXS changes as a function of the Hall carrier density when P3HT (pristine, black circle) is doped using DDB-F_{72}, DDB-F_{36}, F_4TCNQ, and via anion exchange. Table 1 summarizes the R_g values for samples doped at a carrier density of $\sim 5 \times 10^{20}$ cm^{-3}. Most dopants produced smaller domains upon doping, but anion-exchanged samples show larger domains because of doping-induced crystallization of the amorphous parts of the film.

and lowering the average excess energy of the carriers contributing to the transport. As a result, the Seebeck coefficient decreases with increasing doping level, as described by Equation (3). P3HT films doped with F_4TCNQ exhibit the lowest Seebeck coefficient for a given conductivity compared to films doped with the other oxidants. The films doped with DDB-F_{72}, DDB-F_{36}, and via anion-exchange all show a similar (and more favorable) S-σ trend over the measured conductivity range. This indicates that the charge transport efficiency of P3HT films doped with DDBs and via anion-exchange is better than that doped using F_4TCNQ.

Figure 4 also displays fits of the S-σ results to the SLoT model (Equations 2–4); a detailed discussion of these fits and the model is given in the Supporting Information as well as further below. We reiterate that this model assigns charge transport as resulting from an intrinsic conductivity (σ_0) and a carrier-density-dependent localization energy ($W_H(c)$). Although Equation (4) doesn't specify whether σ_0 or $W_H(c)$ has a greater impact on the Seebeck coefficient-conductivity relationship, it is clear that having a higher Seebeck coefficient for a given conductivity level indicates a more favorable doping method.

2.4 | Hall Effect Measurements

To further understand the factors contributing to the S-σ relationship in P3HT doped in different ways, including the carrier mobility, we conducted Hall effect measurements on the same set of samples used for the SLoT fits in Figure 4. A more detailed discussion of the Hall measurements can be found in the SI; the Hall carrier density and mobility as a function of dopant concentration are shown in Figure S10, and an additional comparison supporting the consistency of the Hall-derived carrier densities is shown in Figure S11. Figure 5a shows the measured Hall mobility as a function of the measured Hall carrier density for P3HT films doped with the four different methods. As expected, the Hall carrier mobility generally increases with increasing carrier density due to trap filling and screening effects [17, 18, 78–80]. However, for P3HT films doped with DDB-F_{72} at very high concentrations, the loss of crystallinity leads to a decrease in carrier mobility, as we have noted above and in previous work [8].

Figure 5a also shows that the DDB-F_{72}-, DDB-F_{36}-, and anion-exchange-doped P3HT samples have similar carrier mobilities at the same carrier density. In contrast, the F_4TCNQ-doped samples

exhibit significantly lower mobility at equivalent carrier densities. This fits with the S-σ relationships seen in Figure 4, which indicate that the DDB- and anion-exchange-doped films have better charge transport compared to F_4TCNQ-doped samples. However, this finding poses an interesting question: given that the DDB-based dopants experience reduced Coulomb interactions with the carriers, as indicated by their redshifted P1 absorption and high Hall carrier mobility, why do the anion-exchange-doped P3HT films also exhibit high Hall carrier mobility despite having a bluer P1 peak and thus more localized carriers? Although we previously have argued that a dopant's size, the location of the P1 absorption, and Hall carrier mobility are directly correlated [8, 9], it appears that this is not the case for anion-exchange-doped [28, 30] P3HT. This suggests that other factors, presumably related to the local crystalline and mesoscale morphology, are important to determining the carrier mobility in anion-exchange-doped systems.

One factor that could explain this observation is how different the R_g values are for each dopant, as summarized in Figure 5b. As mentioned above, the larger R_g values for anion exchange likely result from the ability of this method to dope amorphous regions without the large strains associated with DDB insertion into the lattice, leading to the formation of larger, more connected domains. Thus, Figure 5 suggests that the macroscopic charge transport characteristics of P3HT doped with different dopants may be related to the long-range structural ordering in these films, an idea that we explore further below.

2.5 | Probing the Activation Energy, W_H, via Temperature-Dependent Conductivity

Having established the role of dopant-dependent morphology and its impact on Hall carrier mobility, we now turn to temperature-dependent conductivity measurements to examine the energetic landscape of charge transport. Charge transport in semiconducting polymers is often described as hopping between localized states, which requires thermal energy to overcome the barriers between them [18, 81–85]. By measuring the electrical conductivity as a function of temperature ($\sigma(T)$) and fitting the data to the Arrhenius equation, we extract the activation energy, W_H, from the slope of the linear $\ln(\sigma(T))$ versus $(k_B T)^{-1}$ plot to determine how this energy changes with carrier density [82]. Details of the measurement methods and Arrhenius fits are given in the Experimental section (see also Figure S12). The results are shown in Figure 6a,b.

Figure 6a shows that both DDB-F_{72} and DDB-F_{36} doped P3HT films initially experience a sharp decrease in W_H as the Hall carrier density increases. This sharp drop suggests that DDB-doped films have highly delocalized carriers, consistent with the large counterion having reduced Coulomb interaction with the carriers, as evidenced by the red-shifted P1 absorption transition seen in Figure 2. One of the key advantages of using DDB-F_{72} as a dopant, in comparison to DDB-F_{36}, is its strong oxidizing power and higher doping efficiency, which allows us to study the barrier height at very low doping levels. The data suggest that at low doping levels, carriers in DDB-F_{72}-doped P3HT films still experience significant localization despite the weaker Coulomb interactions between the polaron and the dopant counterion.

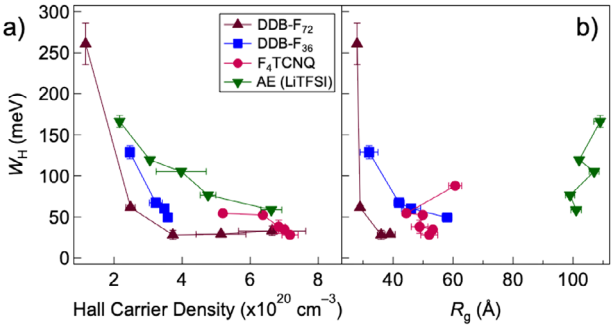

FIGURE 6 | (a) The experimentally-measured activation energy, W_H, for P3HT films doped with different dopants as a function of Hall carrier density. The W_H values are obtained using temperature-dependent conductivity measurements and fitting to the Arrhenius equation. The DDB-based dopants show the fastest drop in W_H upon doping (largest slope) compared to anion-exchange doping or doping with F_4TCNQ. (b) The (general lack of) relation between W_H and R_g from GISAXS.

This localization can be understood by the increased distance between doping sites at low doping levels, leading to poorer overlap between potential wells and thus a higher W_H [18]. Given that the Coulomb interaction with charge carriers is already low in DDB-doped samples, this explains why the decrease in W_H with increasing carrier density is more rapid than with F_4TCNQ- and anion-exchanged doping, where the local Coulomb attraction between carriers and counterions is stronger.

Perhaps the most striking result in Figure 6a, however, is that although the anion-exchange doped samples have relatively high Hall carrier mobilities (Figure 5a) and a favorable Seebeck coefficient-conductivity relationship (Figure 4), they show similar activation energy to the F_4TCNQ-doped samples at the same carrier density. This relatively large W_H, along with the blue-shifted P1 peaks for the AE-doped samples, indicates that the polarons still experience relatively strong Coulomb interactions with the $TFSI^-$ counterions. This again raises the question: why do these samples have high carrier mobilities despite having high activation energies? Normally, a large activation energy would suggest poor carrier mobility, so the better mobility and charge transport must be due to another factor that compensates for the large activation energy.

As mentioned above, we believe that this other factor is related to the mesoscale domain ordering, as quantified by R_g. Figure 6b shows that DDB-F_{72}- and DDB-F_{36}-doped P3HT experience similar W_H barriers, despite having much smaller R_g values compared to F_4TCNQ- and anion-exchange-doped P3HT. This suggests that, for the DDB-doped systems, favorable charge transport is driven primarily by the reduced Coulomb trapping rather than by favorable longer-ranged morphological effects. The one exception to this trend is the most highly-doped DDB-F_{72} sample, which shows a very large domain size and a slightly increased W_H barrier. As discussed above, this overdoped sample is starting to amorphize due to an excess of DDB clusters in the lattice, resulting in reduced domain contrast and thus a larger R_g. In contrast, the anion-exchange-doped P3HT samples exhibit larger R_g values across doping levels, indicating that improved mesoscale connectivity contributes importantly to their favorable long-range transport. These observations therefore suggest that activation energy alone

does not fully determine macroscopic transport. This motivates an analysis of σ_0, the intrinsic conductivity, in Equation (4), which we discuss below.

2.6 | Semi-Localized Transport Model (SLoT)

To better understand the enhanced carrier mobilities and S-σ relation in the AE-doped samples, we next examine the SLoT fits, focusing particularly on the extracted σ_0 values. Within the SLoT framework, σ_0 is the transport prefactor in the absence of localization effects and thus sets the intrinsic conductivity scale of a system. As a result, larger σ_0's correspond to systems that can achieve higher conductivities with a given Seebeck coefficient, even if localization effects are present. The parameters used to fit the SLoT model (Equations 2–4) to the S-σ relationship for the P3HT samples doped at different concentrations with different dopants, shown by the dashed curves in Figure 4, are summarized in Table 1 (see also Table S2).

From these SLoT parameters, we see that P3HT samples doped with DDB-F_{72} and DDB-F_{36} have similar σ_0 values (25 and 35 S cm^{-1}, respectively) and similar rates of change of the localization energy with carrier density ($W_{H,slope}$ = 1000 meV and 1550 meV, respectively). In contrast, the SLoT model fits for the F_4TCNQ- and anion-exchange doped P3HT samples have much smaller $W_{H,slope}$ values (310 meV and 350 meV, respectively), as seen in Figure 6. Additionally, σ_0 increases substantially from 10 S/cm for the F_4TCNQ-doped samples to 125 S/cm for the AE-doped samples; the latter value is 3–4 times higher than the σ_0 values for P3HT doped with the DDB clusters. This suggests that the enhanced charge transport characteristics in the DDB-based doped samples result from both a moderately high σ_0 and a reduced localization energy, while the favorable charge transport characteristics of the anion-exchange-doped samples result from a σ_0 that is so high that it can overcome fairly high localization effects and high activation energies from strong Coulomb interactions.

Given that all the samples we studied in this work are based on the same semiconducting polymer, P3HT, this leads to the question: how can the same doped polymer have such dramatically different intrinsic conductivities simply by changing the dopant or doping method? We find that there is a correlation between the σ_0 parameter obtained from fitting the SLoT model and the mesoscopic degree of order, R_g obtained from GISAXS, as highlighted in Table 1 and Figure 7. This suggests that the dopant's identity, which determines its ability to dope and crystallize certain regions within the P3HT films, thus determining the mesoscale morphology of the doped films, directly influences the charge transport characteristics.

Table 1 and Figure 7 show that although the DDB-based dopants have moderately large values of σ_0, they have smaller R_g values compared to anion-exchange-doped samples. These very small R_g values can be attributed to these dopants' large size, which disrupts the polymer lattice, as seen in Figure 3, leading to shorter long-range structural connectivity between domains. The differences in the σ_0 and R_g values between DDB-F_{72}-doped and DDB-F_{36}-doped P3HT can be explained by the difference in these dopants' oxidizing power. Although DDB-F_{72} can readily dope both crystalline and amorphous regions, its high oxidization

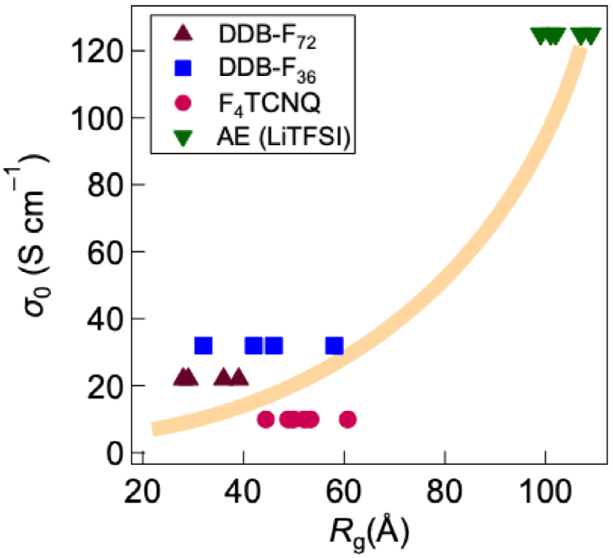

FIGURE 7 | Relationship between σ_0, obtained from SLoT fitting of electrical and thermal measurements, and R_g values, obtained from GISAXS, at all measured carrier densities. The trend indicates that as the domain length increases, the intrinsic conductivity improves proportionally, regardless of the doping level for each dopant. The orange curve is to help guide the eye.

power and large size cause it to overdope the crystalline domains, disrupting the periodicity and resulting in a lower R_g and σ_0. On the other hand, DDB-F_{36}, which is less oxidizing but has an equally large counterion, breaks up the domains less, resulting in a better connectivity between crystalline domains and slightly improved long-range charge transport.

In the case of F_4TCNQ-doped P3HT samples, we attribute the low values of σ_0 and R_g seen in Figures 5b and 7 to the fact that under these conditions, F_4TCNQ predominantly dopes the crystalline regions of P3HT films, creating smaller isolated doped crystalline domains with poorer interdomain transport. In contrast, the anion-exchange-doped P3HT samples exhibit a larger R_g value due to doping-induced crystallization of the amorphous regions without the large lattice strain as seen from the DDB clusters, which expands the connectivity between doped domains and provides for improved long-range charge transport pathways. The large increase in σ_0 observed for the AE-doped samples occurs together with a substantial increase in R_g, suggesting that improved mesoscale ordering and connectivity contribute to the enhanced intrinsic transport scale captured by σ_0. This correlation indicates that the structural reorganization induced by anion exchange favorably modifies the transport landscape of the doped film.

This interpretation is consistent with prior work from both Yamashita and co-workers, who observed enhanced doping levels together with reduced lattice/structural disorder [6, 86], and also Chen et al., who similarly linked charge-transport enhancement with doping-induced ordering of previously less-ordered regions [30]. It is important to note that the SLoT model parameters, including σ_0, are determined entirely from electrical and thermal measurements, while the GISAXS parameters are entirely structurally based, so our results provide perhaps the strongest link

to date between the mesoscale morphology of doped conjugated polymers and thermoelectric properties. From Figure 7, we see that the dopant size, redox potential, and propensity to drive doping-induced crystallization of the amorphous polymer regions are all important for controlling electrical conductivity, since the local and mesoscale structures both directly influence the charge transport characteristics of doped organic semiconducting polymers.

3 | Conclusions

In summary, we explored using four different dopants/doping methods to create doped P3HT films with different morphologies and thus different charge transport characteristics. Hall effect measurements demonstrate that DDB-based dopants and anion-exchange doping provide better charge transport compared to F_4TCNQ, resulting in a better S-σ relationship. The enhanced charge transport observed with DDB-based dopants is attributed to reduced Coulomb interactions and lower activation energy, while anion-exchange doped films and those doped with F_4TCNQ experience strong localization effects and higher activation energy. Hall effect, temperature-dependent conductivity, and UV–vis–NIR spectroscopy probe all show that Coulomb interactions between the dopant counterions and the charge carriers are the dominant factor influencing carrier localization and activation energy in these samples.

Further analysis using the SLoT model indicates that the improvement in charge transport for anion-exchange doping is primarily due to a much higher intrinsic conductivity σ_0 that can compensate for the accompanying higher carrier localization energy ($W_H(c)$). Our structural measurements show that this improvement in the intrinsic conductivity is linked to the doping and ordering of the amorphous regions, improving the R_g and thus the mesoscale charge transport connectivity. All of the results indicate that it is a combination of the local molecular Coulomb interaction, the degree of doping-induced crystallization, and ordering on the mesoscale, which controls overall charge transport in doped conjugated polymer films. Clearly, it is possible to use mesoscale ordering to achieve similar charge transport characteristics even in the presence of strong localization effects, indicating that further research on how to enhance ordering on this length scale is warranted for improving the thermoelectric properties of doped conjugated polymers.

4 | Experimental

4.1 | Device Preparation

Device fabrication was performed on pre-cleaned glass substrates for thermoelectric, electrical, and spectroscopy samples, and on pre-cleaned silicon wafer substrates for GIWAXS and GISAXS samples. The cleaning process involved cutting the substrates into 1.2 × 1.2 cm pieces, followed by sequential washes with Alconox detergent, deionized water, and acetone. After drying with nitrogen gas, the substrates were plasma etched for approximately 10 min. Substrates were transferred to a nitrogen glovebox for spin coating and doping.

P3HT was dissolved in *o*-dichlorobenzene (20 mg/mL) and stirred until fully dissolved. Pristine polymer films were deposited by spin coating at 1000 rpm, followed by a brief high-speed spin step to remove residual solvent. Before doping, films were allowed to crystallize overnight under an inert nitrogen atmosphere. For the sequential doping procedure, the pristine P3HT polymer films were exposed to a dopant solution for a set time period before spin coating at 4000 rpm for 10 s to remove any residual dopant solution. For F_4TCNQ, DDB-F_{72}, and DDB-$F_{36,}$ the dopants were dissolved in dichloromethane (DCM) at the specified concentrations, and the polymer films were then exposed to the corresponding solution for 10 s before spin coating. For anion-exchange-doped samples, various concentrations of F_4TCNQ were dissolved in *n*-butylacetate (*n*-BA) and mixed with an equal volume of 209.0 mM LiTFSI (in *n*-BA) solution to obtain anion-exchange solutions with varying F_4TCNQ concentrations while keeping the LiTFSI concentration constant (104.5 mM). The polymer films were exposed to the dopant solution for 80 s before spin coating.

4.2 | Film Characterization

GIWAXS measurements were performed at the Stanford Synchrotron Radiation Lightsource (SSRL) on beamline 11–3 using an X-ray energy of 12.7 keV at an incidence angle of 0.12°. Diffraction patterns were collected in a helium chamber to increase signal-to-noise with a sample to detector distance of 250 mm and a spot size of ∼150 μm on the image plate. Igor macro Nika was used to calibrate the 2D spectra. WAXStool and Nika were used to reduce the raw data. To ensure reproducibility, all samples were made and measured in triplicate.

GISAXS was collected at the Stanford Synchrotron Radiation Lightsource using beamline 1–5. The scattering X-rays with an incident energy set at 12 keV were collected using a 2D detector at a sample-to-detector distance of 3 meters. The incident angle was set to 0.12°. The 1D integrations were obtained by horizontally integrating near the Yoneda band and were fit using the Unified Fit method from the Irena and Nika package in Igor software. To ensure reproducibility, all samples were made and measured in triplicate.

Conductivity, Hall effect, temperature-dependent conductivity, and NIR–UV–vis spectroscopy measurements were all performed on the same samples. Conductivity was measured by determining the sheet resistance using a Lakeshore MeasureReady M91 FastHall instrument. Film thicknesses were measured with a Dektak 150 stylus profilometer. The samples had 1 × 1 mm square Au electrodes, 50 nm thick, thermally evaporated onto the corners using a 3D-printed shadow mask in an Angstrom Engineering Nexdep thermal evaporator. To ensure reproducibility, all conductivity measurements were conducted on three independent samples.

Hall effect measurements were performed using the same Lakeshore instrument, with a source current of 10 μA and a magnetic field of 1.0236 T; these measurements were conducted on at least three independent samples for reproducibility. Temperature-dependent conductivity was determined by measuring the sample sheet resistance as a function of temperature in a custom-built

Van der Pauw setup using a Keithley 2400 Sourcemeter controlled by LabVIEW software. A Peltier plate controlled the sample temperature, measured by an RTD sensor. UV–vis–NIR spectra were obtained using a JASCO V-770 spectrophotometer.

The Seebeck coefficient was measured on a separate device with a different electrode geometry, consisting of electrodes made from two parallel gold rectangles (10 × 1 mm, 45 nm thick) spaced 10 mm apart. Measurements were performed using a custom-built setup with two Peltier plates to generate a temperature gradient, and the films' temperature gradient was monitored with two RTD sensors. Samples for Seebeck measurements were prepared with the same solutions and at the same time as those used for sheet resistance/Hall/temperature-dependent conductivity/UV–vis–NIR measurements to ensure that all samples were as identical as possible. All Seebeck measurements were conducted on at least three separate samples to ensure reproducibility.

Acknowledgements

This work was supported by the National Science Foundation under grants DMR-2513790 and CHE-2305152. GIWAXS and GISAXS data present in this work made use of facilities at beamline 11–3 and beamline 1–5 at the Stanford Synchrotron Radiation Lightsource. Use of the Stanford Synchrotron Radiation Lightsource, SLAC National Accelerator Laboratory, is supported by the U.S. Department of Energy, Office of Science, Office of Basic Energy Sciences under Contract No. DE-AC02-76SF00515. The authors thank Dr. Sarah A. Hesse, Dr. Nicholas A. Strange, Dr. Olga Kraynis, and Dr. Partha P. Paul for help with beamline setup.

Conflicts of Interest

The authors declare no conflicts of interest.

Data Availability Statement

The data that support the findings of this study are available from the corresponding author upon reasonable request.

References

1. T. M. Swager, "50th Anniversary Perspective: Conducting/Semiconducting Conjugated Polymers. A Personal Perspective on the Past and the Future," *Macromolecules* 50 (2017): 4867–4886, https://doi.org/10.1021/acs.macromol.7b00582.

2. N. Dubey and M. Leclerc, "Conducting Polymers: Efficient Thermoelectric Materials," *Journal of Polymer Science Part B: Polymer Physics* 49 (2011): 467–475, https://doi.org/10.1002/polb.22206.

3. G.-H. Kim, L. Shao, K. Zhang, and K. P. Pipe, "Engineered Doping of Organic Semiconductors for Enhanced Thermoelectric Efficiency," *Nature Materials* 12 (2013): 719–723, https://doi.org/10.1038/nmat3635.

4. J. Tang, Y.-H. Pai, and Z. Liang, "Strategic Insights Into Semiconducting Polymer Thermoelectrics by Leveraging Molecular Structures and Chemical Doping," *ACS Energy Letters* 7 (2022): 4299–4324, https://doi.org/10.1021/acsenergylett.2c02119.

5. E. E. Havinga, W. ten Hoeve, and H. Wynberg, "A New Class of Small Band Gap Organic Polymer Conductors," *Polymer Bulletin* 29 (1992): 119–126, https://doi.org/10.1007/BF00558045.

6. Y. Yamashita, J. Tsurumi, M. Ohno, et al., "Efficient Molecular Doping of Polymeric Semiconductors Driven by Anion Exchange," *Nature* 572 (2019): 634–638, https://doi.org/10.1038/s41586-019-1504-9.

7. I. McCulloch, M. Heeney, C. Bailey, et al., "Liquid-Crystalline Semiconducting Polymers with High Charge-Carrier Mobility," *Nature Materials* 5 (2006): 328–333, https://doi.org/10.1038/nmat1612.

8. T. J. Aubry, K. J. Winchell, C. Z. Salamat, et al., "Tunable Dopants with Intrinsic Counterion Separation Reveal the Effects of Electron Affinity on Dopant Intercalation and Free Carrier Production in Sequentially Doped Conjugated Polymer Films," *Advanced Functional Materials* 30 (2020): 2001800, https://doi.org/10.1002/adfm.202001800.

9. T. J. Aubry, J. C. Axtell, V. M. Basile, et al., "Dodecaborane-Based Dopants Designed to Shield Anion Electrostatics Lead to Increased Carrier Mobility in a Doped Conjugated Polymer," *Advanced Materials* 31 (2019): 1805647, https://doi.org/10.1002/adma.201805647.

10. B. Lüssem, C.-M. Keum, D. Kasemann, B. Naab, Z. Bao, and K. Leo, "Doped Organic Transistors," *Chemical Reviews* 116 (2016): 13714.

11. S. D. Kang and G. J. Snyder, "Charge-Transport Model for Conducting Polymers," *Nature Materials* 16 (2017): 252–257, https://doi.org/10.1038/nmat4784.

12. V. Untilova, J. Hynynen, A. I. Hofmann, et al., "High Thermoelectric Power Factor of Poly(3-hexylthiophene) Through In-Plane Alignment and Doping with a Molybdenum Dithiolene Complex," *Macromolecules* 53 (2020): 6314–6321, https://doi.org/10.1021/acs.macromol.0c01223.

13. Y. Xuan, X. Liu, S. Desbief, et al., "Thermoelectric Properties of Conducting Polymers: The Case of Poly(3-hexylthiophene)," *Physical Review B* 82 (2010): 115454, https://doi.org/10.1103/PhysRevB.82.115454.

14. M. Statz, D. Venkateshvaran, X. Jiao, et al., "On the Manifestation of Electron-Electron Interactions in the Thermoelectric Response of Semicrystalline Conjugated Polymers with Low Energetic Disorder," *Communications Physics* 1 (2018): 16, https://doi.org/10.1038/s42005-018-0016-5.

15. O. Bubnova, Z. U. Khan, A. Malti, et al., "Optimization of the Thermoelectric Figure of Merit in the Conducting Polymer Poly(3,4-ethylenedioxythiophene)," *Nature Materials* 10 (2011): 429–433, https://doi.org/10.1038/nmat3012.

16. Y. Zhong, V. Untilova, D. Muller, et al., "Preferential Location of Dopants in the Amorphous Phase of Oriented Regioregular Poly(3-hexylthiophene-2,5-diyl) Films Helps Reach Charge Conductivities of 3000 S cm^{-1}," *Advanced Functional Materials* 32 (2022): 2202075, https://doi.org/10.1002/adfm.202202075.

17. S. A. Gregory, A. Atassi, J. F. Ponder Jr., et al., "Quantifying Charge Carrier Localization in PBTTT Using Thermoelectric and Spectroscopic Techniques," *The Journal of Physical Chemistry C* 127 (2023): 12206–12217, https://doi.org/10.1021/acs.jpcc.3c01152.

18. S. A. Gregory, R. Hanus, A. Atassi, et al., "Quantifying Charge Carrier Localization in Chemically Doped Semiconducting Polymers," *Nature Materials* 20 (2021): 1414–1421, https://doi.org/10.1038/s41563-021-01008-0.

19. M. G. Voss, D. T. Scholes, J. R. Challa, and B. J. Schwartz, "Ultrafast Transient Absorption Spectroscopy of Doped P3HT Films: Distinguishing Free and Trapped Polarons," *Faraday Discussions* 216 (2019): 339–362, https://doi.org/10.1039/C8FD00210J.

20. D. T. Scholes, P. Y. Yee, J. R. Lindemuth, et al., "The Effects of Crystallinity on Charge Transport and the Structure of Sequentially Processed F_4TCNQ-Doped Conjugated Polymer Films," *Advanced Functional Materials* 27 (2017): 1702654, https://doi.org/10.1002/adfm.201702654.

21. D. T. Scholes, P. Y. Yee, G. R. McKeown, et al., "Designing Conjugated Polymers for Molecular Doping: The Roles of Crystallinity, Swelling, and Conductivity in Sequentially-Doped Selenophene-Based Copolymers," *Chemistry of Materials* 31 (2019): 73–82, https://doi.org/10.1021/acs.chemmater.8b02648.

22. V. Untilova, T. Biskup, L. Biniek, V. Vijayakumar, and M. Brinkmann, "Control of Chain Alignment and Crystallization Helps Enhance Charge Conductivities and Thermoelectric Power Factors in Sequentially Doped

P3HT:F_4TCNQ Films," *Macromolecules* 53 (2020): 2441–2453, https://doi.org/10.1021/acs.macromol.9b02389.

23. Y.-J. Heo, H.-G. Jeong, J. Kim, et al., "Formation of Large Crystalline Domains in a Semiconducting Polymer With Semi-fluorinated Alkyl Side Chains and Application to High-Performance Thin-Film Transistors," *ACS Applied Materials & Interfaces* 12 (2020): 49886–49894, https://doi.org/10.1021/acsami.0c13176.

24. Y.-J. Kim, N.-K. Kim, W.-T. Park, C. Liu, Y.-Y. Noh, and D.-Y. Kim, "Kinetically Controlled Crystallization in Conjugated Polymer Films for High-Performance Organic Field-Effect Transistors," *Advanced Functional Materials* 29 (2019): 1807786, https://doi.org/10.1002/adfm.201807786.

25. J. Mei, D. H. Kim, A. L. Ayzner, M. F. Toney, and Z. Bao, "Siloxane-Terminated Solubilizing Side Chains: Bringing Conjugated Polymer Backbones Closer and Boosting Hole Mobilities in Thin-Film Transistors," *Journal of the American Chemical Society* 133 (2011): 20130–20133, https://doi.org/10.1021/ja209328m.

26. Z. Liang, Y. Zhang, M. Souri, et al., "Influence of Dopant Size and Electron Affinity on the Electrical Conductivity and Thermoelectric Properties of a Series of Conjugated Polymers," *Journal of Materials Chemistry A* 6 (2018): 16495–16505, https://doi.org/10.1039/C8TA05922E.

27. I. E. Jacobs, G. D'Avino, V. Lemaur, et al., "Structural and Dynamic Disorder, Not Ionic Trapping, Controls Charge Transport in Highly Doped Conducting Polymers," *Journal of the American Chemical Society* 144 (2022): 3005–3019, https://doi.org/10.1021/jacs.1c10651.

28. E. M. Thomas, K. A. Peterson, A. H. Balzer, et al., "Effects of Counter-Ion Size on Delocalization of Carriers and Stability of Doped Semiconducting Polymers," *Advanced Electronic Materials* 6 (2020): 2000595, https://doi.org/10.1002/aelm.202000595.

29. M. Lu-Díaz, M. Duhandžić, S. Harrity, S. Samanta, Z. Akšamija, and D. Venkataraman, "Dopant-Induced Energetic Disorder in Conjugated Polymers: Determinant Roles of Polymer–Dopant Distance and Composite Electronic Structures," *Journal of Physical Chemistry C* 128 (2024): 5996.

30. C. Chen, I. E. Jacobs, K. Kang, et al., "Observation of Weak Counterion Size Dependence of Thermoelectric Transport in Ion Exchange Doped Conducting Polymers Across a Wide Range of Conductivities," *Advanced Energy Materials* 13 (2023): 2202797, https://doi.org/10.1002/aenm.202202797.

31. K.-H. Yim, G. L. Whiting, C. E. Murphy, et al., "Controlling Electrical Properties of Conjugated Polymers via a Solution-Based p-Type Doping," *Advanced Materials* 20 (2008): 3319–3324, https://doi.org/10.1002/adma.200800735.

32. C. Y. Kao, B. Lee, L. S. Wielunski, et al., "Doping of Conjugated Polythiophenes with Alkyl Silanes," *Advanced Functional Materials* 19 (2009): 1906–1911, https://doi.org/10.1002/adfm.200900120.

33. J. Yamamoto and Y. Furukawa, "Electronic and Vibrational Spectra of Positive Polarons and Bipolarons in Regioregular Poly(3-hexylthiophene) Doped with Ferric Chloride," *The Journal of Physical Chemistry B* 119 (2015): 4788–4794, https://doi.org/10.1021/jp512654b.

34. V. A. Kolesov, C. Fuentes-Hernandez, W.-F. Chou, et al., "Solution-Based Electrical Doping of Semiconducting Polymer Films over a Limited Depth," *Nature Materials* 16 (2017): 474–480, https://doi.org/10.1038/nmat4818.

35. G. Lu, J. Blakesley, S. Himmelberger, et al., "Moderate Doping Leads to High Performance of Semiconductor/Insulator Polymer Blend Transistors," *Nature Communications* 4 (2013): 1588, https://doi.org/10.1038/ncomms2587.

36. A. M. Glaudell, J. E. Cochran, S. N. Patel, and M. L. Chabinyc, "Impact of the Doping Method on Conductivity and Thermopower in Semiconducting Polythiophenes," *Advanced Energy Materials* 5 (2015): 1401072, https://doi.org/10.1002/aenm.201401072.

37. O. Khatib, B. Lee, J. Yuen, et al., "Infrared Signatures of High Carrier Densities Induced in Semiconducting Poly(3-hexylthiophene) by Fluorinated Organosilane Molecules," *Journal of Applied Physics* 107 (2010): 123702, https://doi.org/10.1063/1.3436567.

38. S. Himmelberger, D. T. Duong, J. E. Northrup, et al., "Role of Side-Chain Branching on Thin-Film Structure and Electronic Properties of Polythiophenes," *Advanced Functional Materials* 25 (2015): 2616–2624, https://doi.org/10.1002/adfm.201500101.

39. A. Hamidi-Sakr, L. Biniek, J.-L. Bantignies, et al., "A Versatile Method to Fabricate Highly In-Plane Aligned Conducting Polymer Films with Anisotropic Charge Transport and Thermoelectric Properties: The Key Role of Alkyl Side Chain Layers on the Doping Mechanism," *Advanced Functional Materials* 27 (2017): 1700173, https://doi.org/10.1002/adfm.201700173.

40. D. Neusser, C. Malacrida, M. Kern, Y. M. Gross, J. van Slageren, and S. Ludwigs, "High Conductivities of Disordered P3HT Films by an Electrochemical Doping Strategy," *Chemistry of Materials* 32 (2020): 6003–6013, https://doi.org/10.1021/acs.chemmater.0c01293.

41. Y. Wu, Q. M. Duong, A. F. Simafranca, C. Z. Salamat, B. J. Schwartz, and S. H. Tolbert, "Crystal Structure Control of the Energetics of Chemical Doping in Rub-Aligned P3HT Films," *ACS Materials Letters* 6 (2024): 489–497, https://doi.org/10.1021/acsmaterialslett.3c01543.

42. K. E. Watts, B. Neelamraju, E. L. Ratcliff, and J. E. Pemberton, "Stability of Charge Transfer States in F_4TCNQ-Doped P3HT," *Chemistry of Materials* 31 (2019): 6986–6994, https://doi.org/10.1021/acs.chemmater.9b01549.

43. V. Untilova, H. Zeng, P. Durand, L. Herrmann, N. Leclerc, and M. Brinkmann, "Intercalation and Ordering of F_6TCNNQ and F_4TCNQ Dopants in Regioregular Poly(3-hexylthiophene) Crystals: Impact on Anisotropic Thermoelectric Properties of Oriented Thin Films," *Macromolecules* 54 (2021): 6073–6084, https://doi.org/10.1021/acs.macromol.1c00554.

44. J. Hynynen, D. Kiefer, and C. Müller, "Influence of Crystallinity on the Thermoelectric Power Factor of P3HT Vapour-Doped with F4TCNQ," *RSC Advances* 8 (2018): 1593.

45. P. Pingel and D. Neher, "Comprehensive Picture of p -type Doping of P3HT with the Molecular Acceptor F_4TCNQ," *Physical Review B* 87 (2013): 115209, https://doi.org/10.1103/PhysRevB.87.115209.

46. A. R. Chew, R. Ghosh, Z. Shang, F. C. Spano, and A. Salleo, "Sequential Doping Reveals the Importance of Amorphous Chain Rigidity in Charge Transport of Semi-Crystalline Polymers," *The Journal of Physical Chemistry Letters* 8 (2017): 4974–4980, https://doi.org/10.1021/acs.jpclett.7b01989.

47. I. E. Jacobs, E. W. Aasen, J. L. Oliveira, et al., "Comparison of Solution-Mixed and Sequentially Processed P3HT:F_4TCNQ Films: Effect of Doping-Induced Aggregation on Film Morphology," *Journal of Materials Chemistry C* 4 (2016): 3454–3466, https://doi.org/10.1039/C5TC04207K.

48. D. A. Stanfield, Y. Wu, S. H. Tolbert, and B. J. Schwartz, "Controlling the Formation of Charge Transfer Complexes in Chemically Doped Semiconducting Polymers," *Chemistry of Materials* 33 (2021): 2343–2356, https://doi.org/10.1021/acs.chemmater.0c04471.

49. K. Wu, C. Z. Salamat, S. H. Tolbert, and B. J. Schwartz, "Molecular Dynamics Study of the Thermodynamics of Integer Charge Transfer vs Charge-Transfer Complex Formation in Doped Conjugated Polymers," *ACS Applied Materials & Interfaces* 14 (2022): 26988–27001, https://doi.org/10.1021/acsami.2c06449.

50. D. A. Stanfield, Z. Mehmedović, and B. J. Schwartz, "Vibrational Stark Effect Mapping of Polaron Delocalization in Chemically Doped Conjugated Polymers," *Chemistry of Materials* 33 (2021): 8489–8500, https://doi.org/10.1021/acs.chemmater.1c02934.

51. Y. Wu, C. Z. Salamat, A. León Ruiz, et al., "Using Bulky Dodecaborane-Based Dopants to Produce Mobile Charge Carriers in Amorphous Semiconducting Polymers," *Chemistry of Materials* 36 (2024): 5552–5562, https://doi.org/10.1021/acs.chemmater.4c00502.

52. A. L. Ayzner, C. J. Tassone, S. H. Tolbert, and B. J. Schwartz, "Reappraising the Need for Bulk Heterojunctions in Polymer–Fullerene

Photovoltaics: The Role of Carrier Transport in All-Solution-Processed P3HT/PCBM Bilayer Solar Cells," *The Journal of Physical Chemistry C* 113 (2009): 20050–20060, https://doi.org/10.1021/jp9050897.

53. S. A. Hawks, J. C. Aguirre, L. T. Schelhas, et al., "Comparing Matched Polymer:Fullerene Solar Cells Made by Solution-Sequential Processing and Traditional Blend Casting: Nanoscale Structure and Device Performance," *The Journal of Physical Chemistry C* 118 (2014): 17413–17425, https://doi.org/10.1021/jp504560r.

54. J. C. Aguirre, S. A. Hawks, A. S. Ferreira, et al., "Sequential Processing for Organic Photovoltaics: Design Rules for Morphology Control by Tailored Semi-Orthogonal Solvent Blends," *Advanced Energy Materials* 5 (2015): 1402020, https://doi.org/10.1002/aenm.201402020.

55. D. T. Scholes, S. A. Hawks, P. Y. Yee, et al., "Overcoming Film Quality Issues for Conjugated Polymers Doped with F_4TCNQ by Solution Sequential Processing: Hall Effect, Structural, and Optical Measurements," *The Journal of Physical Chemistry Letters* 6 (2015): 4786–4793, https://doi.org/10.1021/acs.jpclett.5b02332.

56. T. H. Le, A. Nafady, X. Qu, L. L. Martin, and A. M. Bond, "Detailed Electrochemical Analysis of the Redox Chemistry of Tetrafluorotetracyanoquinodimethane $TCNQF_4$, the Radical Anion $[TCNQF_4]^{\bullet-}$, and the Dianion $[TCNQF_4]^{2-}$ in the Presence of Trifluoroacetic Acid," *Analytical Chemistry* 83 (2011): 6731–6737, https://doi.org/10.1021/ac201373d.

57. Q. M. Duong, D. Garcia Vidales, C. Z. Salamat, S. H. Tolbert, and B. J. Schwartz, "Measuring the Anisotropic Conductivity of Rub-Aligned Doped Semiconducting Polymer Films: The Role of Electrode Geometry," *Physical Review Applied* 21 (2024): 024006, https://doi.org/10.1103/PhysRevApplied.21.024006.

58. E. C. Wu, D. G. Vidales, C. Z. Salamat, et al., "Ultrafast Transient Absorption Studies of the Dynamics of Free and Coulombically Trapped Polarons in Doped Conjugated Polymers," *Advanced Functional Materials* 35 (2025): 07480, https://doi.org/10.1002/adfm.202507480.

59. E. C. Wu and B. J. Schwartz, "Does the Traditional Band Picture Describe the Electronic Structure of Doped Conjugated Polymers? TD-DFT and Natural Transition Orbital Study of Doped P3HT," *Journal of Chemical Theory and Computation* 19 (2023): 6761–6769, https://doi.org/10.1021/acs.jctc.3c00743.

60. E. C. Wu and B. J. Schwartz, "Does the Traditional Band Picture Correctly Describe the Electronic Structure of n-Doped Conjugated Polymers? A TD-DFT and Natural Transition Orbital Study," *Journal of Chemical Theory and Computation* 20 (2024): 10059–10070, https://doi.org/10.1021/acs.jctc.4c00817.

61. A. R. Umar and C. Grieco, "Reevaluating Infrared Spectroscopic Signatures of Polaron Trapping in a Chemically Doped Conducting Polymer," *The Journal of Chemical Physics* 162 (2025): 054720, https://doi.org/10.1063/5.0250708.

62. A. R. Umar, A. L. Dorris, and C. Grieco, "Photoexcited Polaron Relaxation as a Structurally Sensitive Reporter of Charge Trapping in a Conducting Polymer," *Advanced Functional Materials* 34 (2024): 2407181, https://doi.org/10.1002/adfm.202407181.

63. A. R. Umar, A. L. Dorris, N. B. Kotadiya, N. C. Giebink, G. S. Collier, and C. Grieco, "Probing Polaron Environment in a Doped Polymer via the Photoinduced Stark Effect," *The Journal of Physical Chemistry C* 127 (2023): 9498–9508, https://doi.org/10.1021/acs.jpcc.3c01364.

64. R. Ghosh, C. M. Pochas, and F. C. Spano, "Polaron Delocalization in Conjugated Polymer Films," *The Journal of Physical Chemistry C* 120 (2016): 11394–11406, https://doi.org/10.1021/acs.jpcc.6b02917.

65. P. Walter, M. Ilchen, J. Roeh, W. Ohm, C. B. Zeuthen, and U. Klemradt, "In Situ X-ray Measurements to Follow the Crystallization of $BaTiO_3$ Thin Films during RF-Magnetron Sputter Deposition," *Applied Sciences* 11 (2021): 8970.

66. H. V. Sureka, A. C. Obermeyer, R. J. Flores, and B. D. Olsen, "Catalytic Biosensors From Complex Coacervate Core Micelle (C3M) Thin Films," *ACS Applied Materials & Interfaces* 11 (2019): 32354–32365, https://doi.org/10.1021/acsami.9b08478.

67. G. Freychet, M. Maret, M. Fernandez-Regulez, et al., "Morphology of Poly(lactide)- Block -Poly(dimethylsiloxane)- Block -Polylactide High- χ Triblock Copolymer Film Studied by Grazing Incidence Small-Angle X-ray Scattering," *Journal of Polymer Science* 58 (2020): 2041–2050, https://doi.org/10.1002/pol.20200196.

68. C. Darko, I. Botiz, G. Reiter, et al., "Crystallization in Diblock Copolymer Thin Films at Different Degrees of Supercooling," *Physical Review E* 79 (2009): 041802, https://doi.org/10.1103/PhysRevE.79.041802.

69. Y. She, J. Lee, B. T. Diroll, et al., "Rapid Synthesis of Nanoporous Conformal Coatings via Plasma-Enhanced Sequential Infiltration of a Polymer Template," *ACS Omega* 2 (2017): 7812–7819.

70. D.-M. Smilgies, "GISAXS: A Versatile Tool to Assess Structure and Self-Assembly Kinetics in Block Copolymer Thin Films," *Journal of Polymer Science* 60 (2022): 1023–1041, https://doi.org/10.1002/pol.20210244.

71. G. Santoro, S. Yu, G. Santoro, and S. Yu, *X-ray Scattering*, ed. A. E. Ares, (IntechOpen, 2017), 29–60, https://doi.org/10.5772/64877.

72. G. Beaucage, "Approximations Leading to a Unified Exponential/Power-Law Approach to Small-Angle Scattering," *Journal of Applied Crystallography* 28 (1995): 717–728, https://doi.org/10.1107/S0021889895005292.

73. S. Lenz, M. Bonini, S. K. Nett, et al., "Global Scattering Functions: A Tool for Grazing Incidence Small Angle X-Ray Scattering (GISAXS) Data Analysis of Low Correlated Lateral Structures," *The European Physical Journal Applied Physics* 51 (2010): 10601, https://doi.org/10.1051/epjap/2010064.

74. X. Yan, M. Xiong, X.-Y. Deng, et al., "Approaching Disorder-Tolerant Semiconducting Polymers," *Nature Communications* 12 (2021): 5723, https://doi.org/10.1038/s41467-021-26043-y.

75. J. Rivnay, R. Noriega, R. J. Kline, A. Salleo, and M. F. Toney, "Quantitative Analysis of Lattice Disorder and Crystallite Size in Organic Semiconductor Thin Films," *Physical Review B* 84 (2011): 045203, https://doi.org/10.1103/PhysRevB.84.045203.

76. Z. Peng, L. Ye, and H. Ade, "Understanding, Quantifying, and Controlling the Molecular Ordering of Semiconducting Polymers: From Novices to Experts and Amorphous to Perfect Crystals," *Materials Horizons* 9 (2022): 577–606, https://doi.org/10.1039/D0MH00837K.

77. X. Jiao, M. Statz, L. Lai, et al., "Resolving Different Physical Origins Toward Crystallite Imperfection in Semiconducting Polymers: Crystallite Size vs Paracrystallinity," *The Journal of Physical Chemistry B* 124 (2020): 10529–10538, https://doi.org/10.1021/acs.jpcb.0c06763.

78. R. Warren, P. W. M. Blom, and N. Koch, "Molecular p -Doping Induced Dielectric Constant Increase of Polythiophene Films Determined by Impedance Spectroscopy," *Applied Physics Letters* 122 (2023): 152108, https://doi.org/10.1063/5.0146194.

79. S. P. Schießl, X. de Vries, M. Rother, et al., "Modeling Carrier Density Dependent Charge Transport in Semiconducting Carbon Nanotube Networks," *Physical Review Materials* 1 (2017): 046003.

80. K. N. Baustert, J. H. Bombile, M. T. Rahman, et al., "Combination of Counterion Size and Doping Concentration Determines the Electronic and Thermoelectric Properties of Semiconducting Polymers," *Advanced Materials* 36 (2024): 2313863, https://doi.org/10.1002/adma.202313863.

81. O. Bubnova and X. Crispin, "Towards Polymer-Based Organic Thermoelectric Generators," *Energy & Environmental Science* 5 (2012): 9345, https://doi.org/10.1039/c2ee22777k.

82. M. Schwarze, C. Gaul, R. Scholz, et al., "Molecular Parameters Responsible for Thermally Activated Transport in Doped Organic Semiconductors," *Nature Materials* 18 (2019): 242–248, https://doi.org/10.1038/s41563-018-0277-0.

83. B. A. Gregg, S.-G. Chen, and R. A. Cormier, "Coulomb Forces and Doping in Organic Semiconductors," *Chemistry of Materials* 16 (2004): 4586–4599, https://doi.org/10.1021/cm049625c.

84. R. Noriega, J. Rivnay, K. Vandewal, et al., "A General Relationship Between Disorder, Aggregation and Charge Transport in Conjugated

Polymers," *Nature Materials* 12 (2013): 1038–1044, https://doi.org/10.1038/nmat3722.

85. S. Ihnatsenka, X. Crispin, and I. V. Zozoulenko, "Understanding Hopping Transport and Thermoelectric Properties of Conducting Polymers," *Physical Review B* 92 (2015): 035201, https://doi.org/10.1103/PhysRevB.92.035201.

86. Y. Yamashita, J. Tsurumi, T. Kurosawa, et al., "Supramolecular Cocrystals Built Through Redox-Triggered Ion Intercalation in π-Conjugated Polymers," *Communications Materials* 2 (2021): 45, https://doi.org/10.1038/s43246-021-00148-9.

Supporting Information

Additional supporting information can be found online in the Supporting Information section.

Supporting File: adfm75510-sup-0001-SuppMat.pdf.